GPS Solutions (2025) 29:118
https://doi.org/10.1007/s10291-025-01860-6

RESEARCH

Intelligent detection of traveling ionospheric disturbances from dense GNSS TEC observations utilizing instance segmentation model Cascade Mask R-CNN

Xiaodong Ren[1,3] · Pengchong Zhao[1] · Xuan Le[1] · Linghuo Jian[1] · Ahmed Abdelaziz[4] · Xiaohong Zhang[1,2,3]

Received: 24 October 2024 / Accepted: 8 April 2025 / Published online: 23 May 2025

Abstract

Traveling ionospheric disturbances (TIDs) may significantly change the ionospheric properties in the region, which in turn affects the radio propagation process, especially on short-wave communication, satellite navigation and positioning. TIDs detection and propagation parameter calculation are essential foundations for ionospheric disturbance monitoring and early warning. Comparisons between Cascade Mask R-CNN and the classical Mask R-CNN models in instance segmentation results were conducted using global LSTIDs and European MSTIDs data. The results indicate that Cascade Mask R-CNN outperforms Mask R-CNN in image processing accuracy and training convergence speed, with an improvement of approximately 4.7% in bounding box precision and about 3.6% in mask accuracy. The model achieved mask accuracies of 79.34% and 73.37% in the European region and globally, respectively. Subsequently, irregular disturbances were normalized using a least squares ellipse fitting method, and isolated disturbances were filtered and eliminated using filtering criteria and a nonlinear programming solver. When the filtering threshold T1 was set to 40, isolated disturbances could be effectively filtered out while retaining wave disturbance components. The method yielded TIDs propagation parameters in DTEC maps in different regions that closely matched actual results.

Keywords Traveling ionospheric disturbances (TIDs) · Global navigation satellite system (GNSS) · Ionospheric total electron content (TEC) · Deep learning · Instance segmentation · Cascade Mask R-CNN

Introduction

Traveling ionospheric disturbances (TIDs) are typical disturbances in the ionosphere, characterized by quasi-periodic fluctuations in plasma density and propagating at a certain speed and frequency within the ionosphere (Hines 1960; Kelley 2009). According to their spatial–temporal scales and propagation characteristics, TIDs can mainly be divided into two categories: large-scale traveling ionospheric disturbances (LSTIDs) and medium-scale traveling ionospheric disturbances (MSTIDs). LSTIDs have horizontal wavelengths > 1000 km, horizontal speeds exceeding 400 m/s, and propagation periods ranging from 30 min to 3 h (Hunsucker 1982; Figueiredo et al. 2017). LSTIDs are typically associated with acoustic gravity waves (AGWs) generated by auroral and sub-auroral Joule heating or particle precipitation, propagating from polar regions towards the equator and potentially reaching the opposite hemisphere, thereby affecting the entire globe (Frissell et al. 2022). MSTIDs mainly occur in mid- to low-latitude regions, with horizontal wavelengths of several 1000 km, horizontal speeds ranging from 100 to 250 m/s, and propagation periods of tens of minutes (Huang et al. 2016; Le et al. 2024). MSTIDs are associated with natural hazards such as solar flares, magnetic storms, solar eclipses, earthquakes, tsunamis, typhoons, and volcanic eruptions, as well as phenomena driven by variations in ionizing solar radiation, including solar terminator

✉ Xiaohong Zhang
xhzhang@sgg.whu.edu.cn

1 School of Geodesy and Geomatics, Wuhan University, Wuhan 430079, China

2 Chinese Antarctic Center of Surveying and Mapping, Wuhan University, Wuhan 430079, China

3 Hubei Luojia Laboratory, Wuhan University, Wuhan 430079, China

4 State Key Laboratory of Information Engineering in Surveying, Mapping and Remote Sensing (LIESMARS), Wuhan University, Wuhan 430079, China

passages and solar flares (Koucká Knížová et al. 2021). Both LSTIDs and MSTIDs can significantly alter ionospheric characteristics in their respective regions, severely impacting the reliability and stability of services such as shortwave communication and satellite navigation systems (Zhang et al. 2022; Ren et al. 2024).

Traditional technologies for observing TIDs mainly include ionosondes, high-frequency radars, coherent and incoherent scatter radars, and airglow imagers (Behnke 1979; Kelley 2009; Huang et al. 2016; Ren et al. 2022). Due to their high cost and sparse distribution, these devices can only observe ionospheric structural changes in limited areas, making it difficult to conduct high-precision monitoring under all weather conditions. With the establishment of global navigation satellite systems (GNSS) and the improvement of a dense global GNSS monitoring network, the use of GNSS dual-frequency observations to obtain total electron content (TEC) data has become one of the most widely used methods for monitoring ionospheric disturbance structures (Cherniak and Zakharenkova 2018; Liu et al. 2022; Li and Jiang et al. 2024).

Research on the detection and identification of TIDs using GNSS data can be classified into two main categories. The first category involves using single-station methods to detect ionospheric irregularities, including single-station index such as the Rate of TEC Index (ROTI, Pi et al. 1997), SRMTID index(Hernández-Pajares et al. 2012), DROT index (Efendi and Arikan 2017), DIXSG index (Wilken et al. 2018), ATID index (Borries et al. 2023), IROTI index (Ren et al. 2024), and so on. These indices have gradually enabled the detection of TIDs, but distinguishing between the wave structures of standing waves and TIDs using single-site data remains a challenge. Since natural disasters such as earthquakes and tsunamis often trigger ionospheric disturbances, near-real-time (NRT) TIDs detection has become an effective means of early warning for tsunamis and earthquakes (Kamogawa et al. 2016; Astafyeva 2019; Guerra et al. 2024). In recent years, many researchers have focused on the TID detection. Ravanelli et al. (2021) combined the variometric approach for displacement analysis stand-alone engine (VADASE) with the variometric approach for real-time ionosphere observation (VARION) algorithm to propose a real-time method for tsunami-induced TIDs based on the total variometric approach (TVA). Brissaud and Astafyeva (2022) applied machine learning techniques to separate co-seismic ionospheric disturbances (CIDs) from noise and describe earthquakes and tsunamis in near real-time using CID arrival times. Considering the spatial correlation of disturbance structures, Yang et al. (2023) proposed a method based on wavelet coherence and cross-correlation to detect and analyze ionospheric disturbances induced by earthquakes/tsunamis, which is effectively applicable to large GPS networks in Japan, the United States, and New Zealand. Martire et al. (2023) developed GUARDIAN, a NRT ionospheric monitoring software for natural disaster early warning, which provides NRT TEC time series from multiple GNSS in the Pacific region and inversely estimates tsunami wave parameters. Fuso et al. (2024) utilized machine learning algorithms (random forest and XGBoost) to detect tsunami-induced TIDs using observation values (dSTEC/dt) generated by VARION. Ravanelli et al. (2024) employed deep learning insights to perform automated real-time TID monitoring and detection. By integrating Gramian angular difference fields (GADFs) with convolutional neural networks (CNNs), they used VARION to estimate tsunami-induced TIDs in real-time, validating the method's effectiveness through four tsunami-triggered seismic events. Luhrmann et al. (2022, 2025) proposes a near-real-time method based on an LSTM neural network to detect seismically induced ionospheric disturbances and successfully identifies an anomalous signal following the second earthquake in the 2023 Earthquake Sequence in Turkey.

The second category involves using two-dimensional Differential TEC (DTEC) maps to identify TIDs, allowing direct determination of the occurrence of TID phenomena through 2D images. This method requires sufficiently dense station data, and current identification methods primarily rely on manual judgment. In terms of studying the propagation characteristics of TIDs (speed, period, wavelength, azimuth, etc.), there are two main calculation methods. One method involves frequency domain analysis, which extracts TID frequency and phase differences in specific local regions to invert various propagation parameters of TIDs (Huang et al. 2016). This includes methods such as fast Fourier transform (FFT) and multi-channel maximum entropy method (MMEM) (Huang et al. 2017). However, these methods struggle to accurately remove the Doppler effects of GPS satellites, making it challenging to assess the accuracy of the results (Le et al. 2024). The other method mainly utilizes the temporal changes of two-dimensional DTEC maps to calculate the corresponding propagation parameters of TIDs. For example, Yang et al. (2017) proposed the Atomic Decomposition Detector of MSTIDs (ADDTID), an integrated multi-MSTID detection technique. It was successfully applied to both simulated and real data from extensive and dense networks of GNSS permanent receivers (such as GEONET in Japan) to automatically identify the unique distribution of MSTIDs without the need for visual inspection of VTEC maps. But it faces difficulties when dealing with a large amount of data (Liu et al. 2022).

The rapid development of object detection and image segmentation algorithms in deep learning has made it possible to automate the processing of large amounts of DTEC map data. Girshick (2015) proposed the region-based convolutional neural network (R-CNN) algorithm, which outperformed the traditional deformable part model (DPM)

algorithm in object detection. Subsequently, the series of R-CNN algorithms flourished, with later object detection frameworks such as Fast R-CNN, Faster R-CNN, and instance segmentation framework Mask R-CNN continuously improving the detection speed of images from the initial 2 s per image to several frames per second (Girshick 2015; Ren et al. 2017; He et al. 2017). Liu et al. (2022) introduced Mask R-CNN into MSTID detection and analyzed the climatological characteristics of long-term MSTIDs in Japan and the results showed that Mask R-CNN could intelligently detect MSTIDs with an accuracy of about 80% and a detection speed of approximately 8 frames per second (fps). Lai et al. (2023) analyzed the MSTIDs characteristics in central China using airglow imagers and a CNN-based classification framework.

The above-mentioned deep learning methods typically employ a two-stage approach that combines object detection and segmentation tasks, where separate detection and segmentation tasks can impact image processing performance and target detection accuracy. Therefore, Cai and Vasconcelos (2019) proposed a multi-stage method called Cascade Mask R-CNN to enhance target detection performance. This paper will propose an intelligent detection algorithm for TIDs based on the instance segmentation model and compare the detection performance of Cascade Mask R-CNN and Mask R-CNN for TIDs. The structure is as follows: "Data source and preprocessing" section introduces the data sources and preprocessing steps. "Methodology" section details the principles of the Mask R-CNN and Cascade Mask R-CNN models, as well as the calculation method of MSTIDs propagation parameters. "Results and discussion" section provides a comparative analysis of the experimental results. Finally, "Conclusions" section summarizes the conclusions.

Data source and preprocessing

Currently, there is no publicly available dataset for the intelligent recognition of TIDs. Therefore, this paper creates a dataset using TEC data obtained from the Madrigal distributed data system developed by the Haystack Observatory at the Massachusetts Institute of Technology (Rideout and Coster 2006). This database provides ground-based GNSS slant TEC (STEC) data from approximately 6300 GNSS stations, with a time resolution of 30 s. The detailed process of retrieving TEC from GNSS data can be found in previous studies (Vierinen et al. 2016). We obtain the DTEC sequences by applying a 1-h window Savitzky–Golay (SG) filtering method to the TEC data, excluding satellite signals with elevation angles below 30° (Oludehinwa et al. 2022; Ren et al. 2024). The DTEC data at different time points are visualized as DTEC maps, which are then annotated using the open-source software *Labelme* (https://github.com/wkentaro/labelme). The annotated labels are used as ground truth masks for model training. The dataset created in this study spans the complete solar activity cycle from 2013 to 2023. It includes 50 global-scale DTEC maps capturing LSTIDs primarily triggered by intense geomagnetic storms, and 270 regional-scale DTEC maps over Europe focusing on MSTIDs to enhance the model's generalization capability. All DTEC maps were rigorously selected from the Madrigal database. The sampling strategy accounts for both solar maximum and minimum conditions, ensuring temporal coverage across the entire 24th solar cycle. After establishing the dataset, the selected data is annotated using the image annotation tool *Labelme*. Figure 1 displays the global and European region DTEC maps along with the manually annotated results. Finally, the datasets of LSTIDs and MSTIDs were divided into training and validation sets in a 7:3 ratio for training.

Methodology

Figure 2 illustrates the steps of the TIDs intelligent detection algorithm used in this study. Firstly, two deep learning instance segmentation networks, Cascade Mask R-CNN and Mask R-CNN, are used to intelligently detect the TIDs. Then the boundary ellipse is drawn to normalize the detected wavy structures. Based on the spatial distribution characteristics of TIDs, a filtering criterion can be used to distinguish whether a wavy structure belongs to a TID or not. To prevent a TID waveform structure from being rejected as part of a TID due to certain abnormal features, we use nonlinear optimization tools to determine the threshold for the filtering criteria. Finally, the MSTID features are automatically inferred using the filtering criterion to eliminate isolated wave-like disturbances. Detailed information is further discussed in the following subsections.

Cascade Mask R-CNN model and accuracy evaluation methods

The traditional convolutional neural network (CNN) is used for image classification, providing overall classification predictions based on input images. However, it is not suitable for intelligent detection of TIDs as it cannot extract disturbance information from DTEC maps. Semantic segmentation is a method of classifying each pixel in an image to determine the object or region to which it belongs (Minaee et al. 2022). Semantic segmentation enables pixel-level segmentation of images, providing a foundation for extracting disturbance information from DTEC maps using deep learning methods. However, it overlooks the spatial information

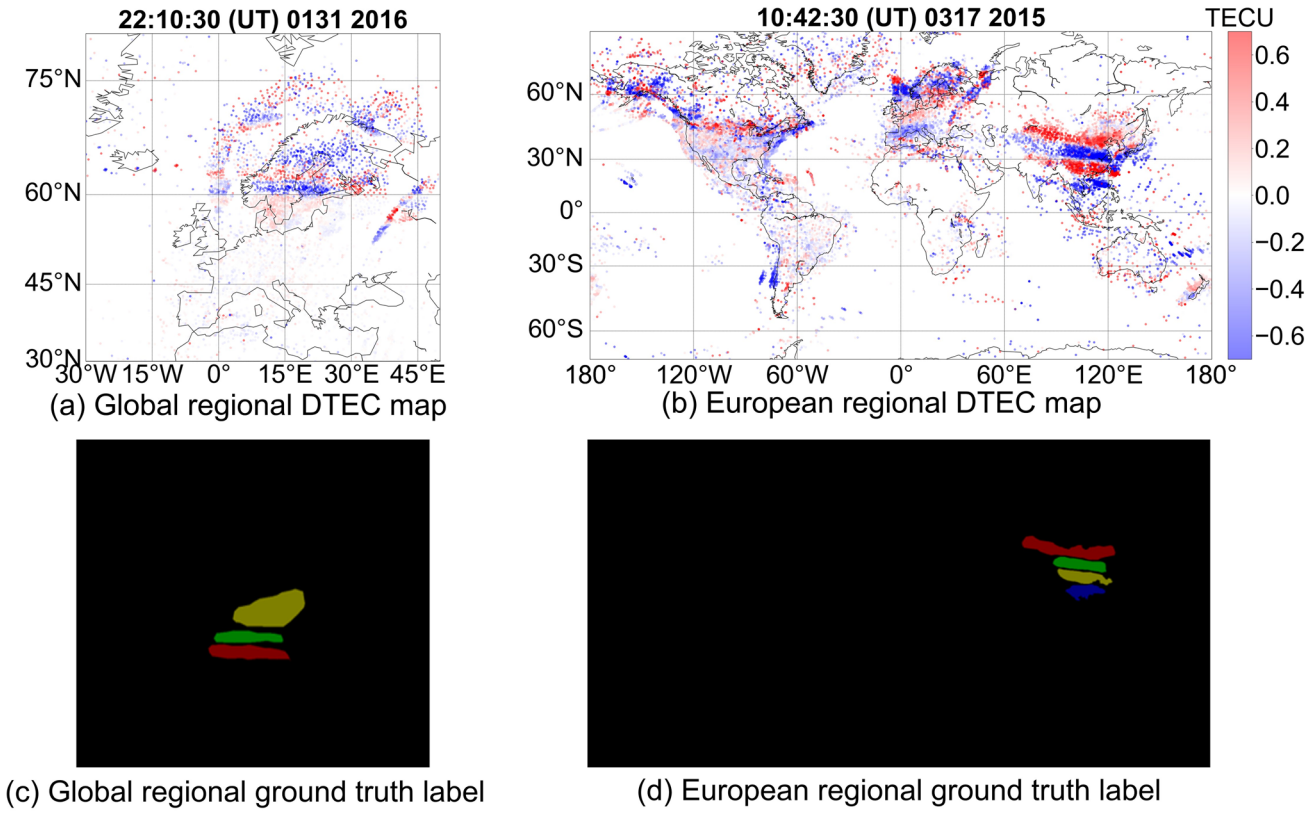

Fig. 1 DTEC maps of the global and European regions with corresponding manually annotated labels

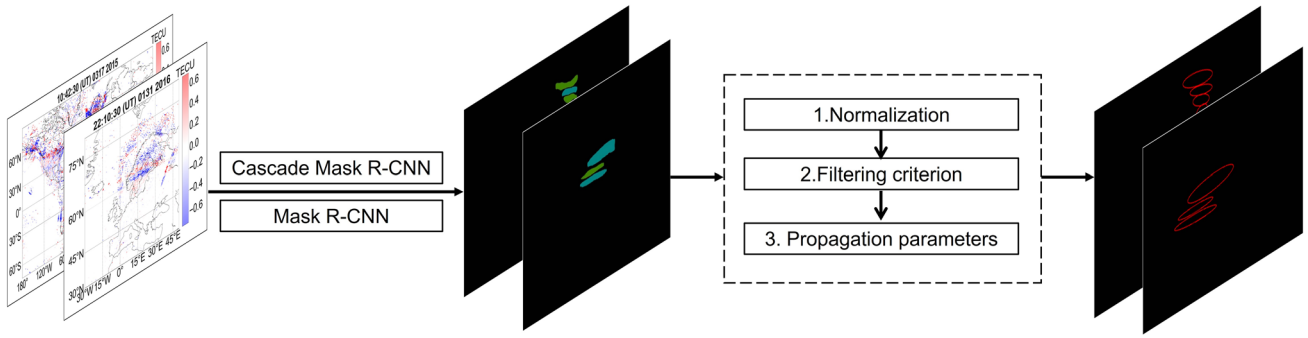

Fig.2 Flow chart of TIDs intelligent detection algorithm proposed in this research

of different individuals belonging to the same category, which hinders the subsequent calculations of TID feature parameters. Instance segmentation is a higher-level task that combines object detection and semantic segmentation. Building upon semantic segmentation, instance segmentation distinguishes different instances of the same category and can be used to detect various types of wave-like disturbances from DTEC maps.

The basic structure of Cascade Mask R-CNN is consistent with Mask R-CNN. Its main structure is shown in Fig. 3, which can be divided into the following parts: backbone, region proposal network (RPN), region of interest (ROI) selection and normalization, and prediction regression.

Backbone

The backbone is a standard CNN convolutional network, typically using ResNet50 or ResNet101, aimed at extracting information features from images. Additionally, it incorporates a feature pyramid network (FPN) designed to address the detection and segmentation challenges of objects at different scales.

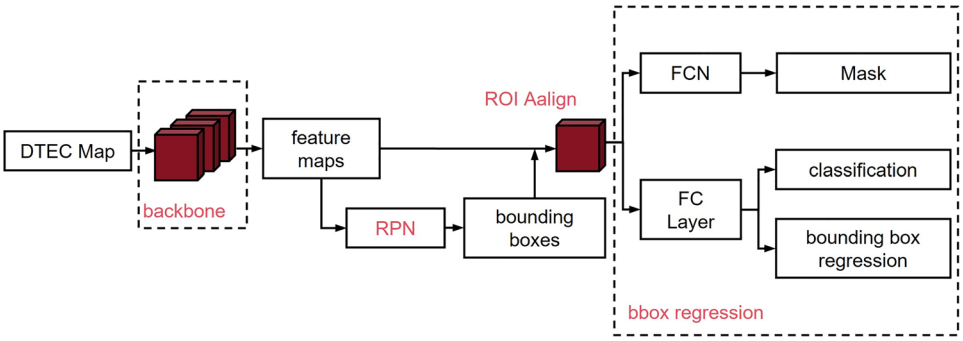

Fig. 3 Schematic structure of Cascade Mask R-CNN and Mask R-CNN

Region proposal network

The RPN layer is an innovative feature of the R-CNN series, used to distinguish and preliminary locate multiple ROI on the feature map. Compared to traditional candidate box selection methods, RPN is more efficient. RPN includes a classifier and regressor that learns where objects are present in the original image and where they are not, making it easier to integrate into the entire network as a cohesive unit.

Region of interest (ROI) selection

The ROI is made up of the feature map produced by the backbone and the candidate boxes generated by the RPN. The main task of the ROI is to map the generated candidate boxes to the feature map.

Prediction regression

Finally, the normalized feature maps of the same ROI are separately input into the traditional CNN branch with fully connected layers for image bounding box prediction and classification, as well as the FCN branch without fully connected layers for pixel-level mask prediction.

Due to the addition of the mask branch, the loss function for each ROI is shown below:

$$L = L_{cls} + L_{box} + L_{mask} \tag{1}$$

where L_{cls} and L_{box} are the regression and classification loss for bounding boxes, respectively; L_{mask} denotes the loss for the mask.

Cascade Mask R-CNN improves upon Mask R-CNN by introducing multiple stages instead of two stages (Cai and Vasconcelos 2019). Figure 4 shows the improved part of Cascade Mask R-CNN over Mask R-CNN. The first stage involves extracting the features of each bounding box by using the bounding box provided by RPN and the feature map output by the backbone network. The second stage involves extracting features of each bounding box using the bounding box B1 generated in the first stage and the feature map output by the backbone network. Similarly, the third stage involves extracting features of each bounding box using the bounding box B2 generated in the second stage and the feature map output by the backbone network.

In the second and third stages of Cascade Mask R-CNN, new detection and segmentation results are predicted based on the results of the previous stage. This approach offers high accuracy but comes with a significant increase in time complexity. When extracting disturbances from DTEC maps, precision is the primary concern rather than processing speed. Therefore, this study chose to use the instance segmentation Cascade Mask R-CNN model. It should be noted that the current model is not yet suitable for real-time or early warning applications and the focus of this work is on accurate post-event detection and characterization of TID.

The second and third stages of Cascade Mask R-CNN predict new detection and segmentation results on top of the previous stage, respectively, and the advantage of this type of method is the higher accuracy, but it will be accompanied

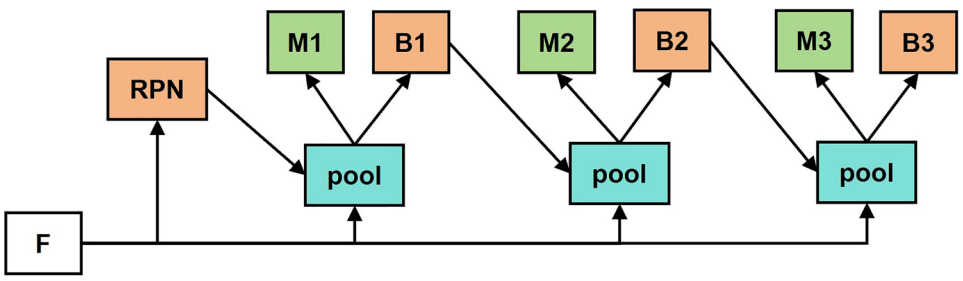

Fig. 4 Improvement of Cascade Mask R-CNN over Mask R-CNN

by a huge time complexity because the extraction of perturbations in the DTEC map only cares about the accuracy and does not care about the speed of the processing, so in this paper, we choose to use the instance segmentation Cascade Mask R-CNN model.

The following describes the model accuracy evaluation methods. average precision (AP) is a metric used to evaluate the performance of deep learning tasks such as target detection and image classification. In target detection tasks, AP is usually used to measure the balance between the accuracy and recall of the model on different categories. Precision is a measure of accuracy with the following formula:

$$Precision = \frac{TP}{TP + FP} \tag{2}$$

where TP stands for true positives, which are the instances correctly classified as positive [intersection over union (IoU) greater than the corresponding threshold]; FP stands for false positives, which are the instances incorrectly classified as positive (IoU less than the corresponding threshold).

Recall is a metric used to evaluate the coverage ability of a classification model in predicting positive class samples, and its formula is as follows:

$$Recall = \frac{TP}{TP + FN} \tag{3}$$

where FN stands for False Negatives, which are instances incorrectly classified as negative, i.e., instances that are actually positive but are classified as negative by the classifier. AP evaluates the performance of a model by calculating the area under the Precision-Recall curve. A larger area indicates better model performance. The formula for AP is as follows:

$$AP = \sum_{i=1}^{n-1} (r_{i+1} - r_i) \cdot P(r_{i+1}) \tag{4}$$

where n is the number of recall rates, r_i denotes the ith recall rate, $P(r_{(i+1)})$ denotes the precision when the recall is r_{i+1}. In object detection tasks, the AP values are typically calculated for each class, and the average of these class-specific AP values is computed to obtain the mean average precision (mAP). mAP is a metric used to comprehensively evaluate the detection accuracy of a model across multiple classes. mAP_{50} represents the mAP value at an IoU threshold of 50%, mAP_{75} represents the mAP value at an IoU threshold of 75%, and $mAP_{50:5:95}$ represents the average mAP value at IoU thresholds of 50%, 55%, 60%, 65%, 70%, 75%, 80%, 85%, 90%, and 95%. mAP_{small} is the mAP value when smaller bounding boxes are selected, mAP_{medium} denotes the mAP value when medium-sized bounding boxes are selected, and mAP_{large} indicates the mAP value when larger bounding boxes are selected.

Mask normalization and isolated disturbance removal method

During the process of extracting ionospheric disturbances in deep learning instance segmentation models, the extracted masks are often irregular in shape. These irregular edge components can pose challenges in distinguishing TIDs from isolated disturbances and in deriving features. Therefore, in such cases, it is necessary to normalize the geometric shapes of the disturbances. In traditional object detection fields, the method of annotating objects involves drawing a bounding box parallel to the image edges. However, this method may falsely label pixels that do not belong to the wave-like disturbance shape, leading to significant errors when calculating the area of the disturbance waveform. Therefore, based on the least squares ellipse fitting method, this study draws a constrained ellipse for each wave-like structure to normalize the geometric shapes of wave disturbances (Liu et al. 2022). Representing disturbance waveforms using ellipse

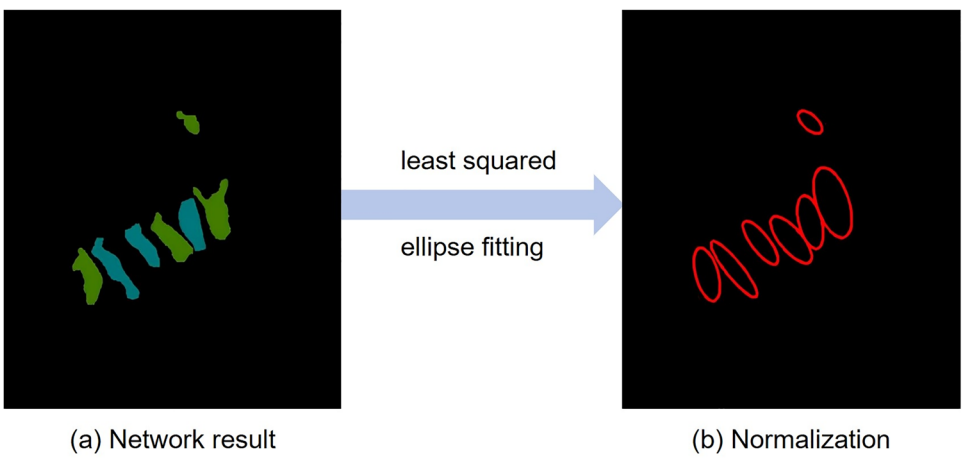

Fig. 5 The effect of normalization of undulating perturbation graphs

parameters facilitates the rapid calculation of subsequent TIDs propagation parameters.

Figure 5 illustrates an example using the graphical normalization method. Figure 5a shows the network's output mask results, which represent the extracted disturbance shapes. Figure 5b displays the image after graphical normalization, where each disturbance shape is represented by the closest fitting ellipse. This approach reduces the number of parameters significantly and facilitates the removal of outliers and TIDs feature calculation in subsequent steps.

To store the disturbance information in the DTEC map, this study selects an $m \times n$ matrix to retain all the disturbance information in one image. The formula expression is as follows:

$$C^t_{m\times n} = \begin{bmatrix} x^t_1 & y^t_1 & a^t_1 & b^t_1 & S^t_1 & \dots & \theta^t_1 \\ x^t_2 & y^t_2 & a^t_2 & b^t_2 & S^t_2 & \dots & \theta^t_2 \\ \vdots & \vdots & \vdots & \vdots & \vdots & \ddots & \vdots \\ x^t_m & y^t_m & a^t_m & b^t_m & S^t_m & \dots & \theta^t_m \end{bmatrix} \tag{5}$$

where m is the total number of ionospheric disturbances extracted, n is the total number of features for each disturbance, and t represents the timestamp of the current DTEC map; each row in the matrix $C^t_{m\times n}$ represents information about a specific disturbance. The study uses a 6-dimensional feature vector ($n=6$) to represent its characteristics, which include the coordinates of the center point (x, y), the major axis of the ellipse a, the minor axis of the ellipse b, the area of the ellipse S, and the angle between the major axis and the north direction θ.

In addition to the TIDs information, isolated wave-like disturbances may also exist and impact the calculation of subsequent TIDs propagation parameters. The spacing between isolated disturbances and TIDs wave-like disturbances is often greater than the spacing between wave-like disturbances within TIDs. Therefore, calculating the n-dimensional Euclidean distance FC_{ij} between the ith and jth disturbances and setting corresponding filtering criteria can help identify isolated disturbances. The filtering criteria can be represented as the minimum weighted n-dimensional Euclidean distance FC_i between the ith and jth disturbances should be less than the threshold T_1 (Liu et al. 2022):

$$FC_i = \underset{i,j\in[1,m],j\neq i}{\text{minimize}} \sum_{k=1}^{n} \left(\frac{C^t_{i,k} - C^t_{j,k}}{O_k} \right)^2 \le T_1 \tag{6}$$

where O_k is a scale normalization term referring to the magnitude of the kth feature. Introducing the scale normalization term helps avoid the dominant impact of excessively large feature parameters on the threshold T_1. When processing the ith normalized disturbance structure in the DTEC map, if there exists a j ($j \in [1, m], j \neq i$) that satisfies the filtering criteria, it is considered a matching pair with the ith disturbance, belonging to the same group of wave-like disturbances. Conversely, the ith disturbance structure is regarded as an isolated disturbance and is removed from the mask image and feature matrix. After completing all iterations for i ($i \in [1, m]$), the remaining disturbance structures in the feature matrix are considered as TIDs information.

Liu et al. (2022) constrained FC based on previous observational results of MSTIDs and derived the value of threshold T1 through an optimization problem (T1 = −39.7659). To validate the effect of the threshold T_1 on the removal of isolated disturbances, this study selected a certain amount of DTEC maps containing MSTIDs events. The FC values for each MSTID structure and isolated disturbance removal in each map were statistically analyzed to observe whether the selection of the threshold T_1 effectively removes isolated disturbances. Figure 6 presents the validation results of the threshold T_1 using a selected number of disturbance events. The x-axis represents different disturbance structure events, while the y-axis represents the FC value corresponding to

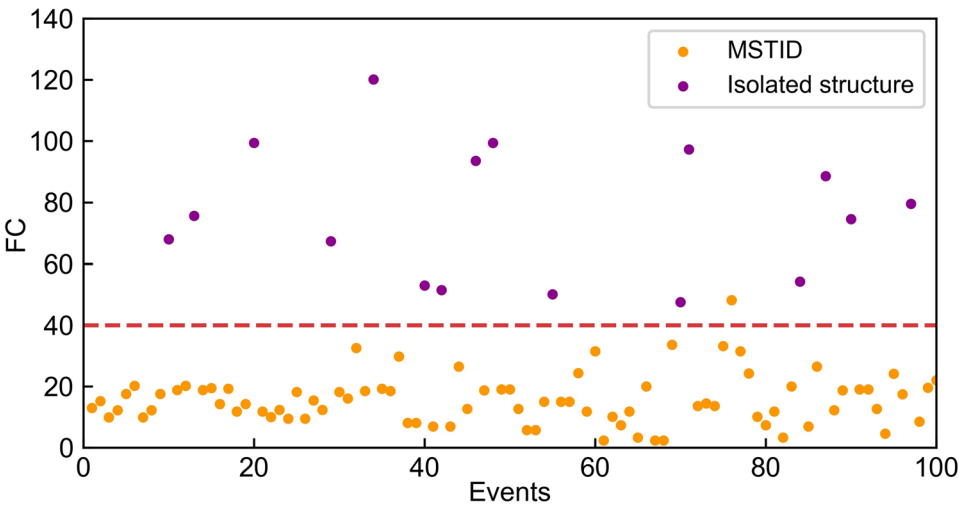

Fig. 6 Statistics of FC values for MSTIDs events and isolated disturbance events

each disturbance. The yellow points in the graph represent MSTIDs, and the purple points represent isolated disturbances that need to be removed. When the threshold T_1 is set to 40, isolated disturbances and MSTIDs are effectively separated. For the 76th disturbance event, the *FC* value of the MSTID exceeds the threshold, indicating that the MSTID structure most closely related to it is at a certain distance away and may not be adjacent. This could introduce errors in propagation parameter calculations; hence, it is also removed. Overall, the *FC* values of MSTIDs are generally concentrated in the range of 10–30, while the FC values of isolated disturbances are mostly above 50. Therefore, when the threshold T_1 is set to 40, this filtering criterion performs well in removing isolated disturbances.

Calculation of propagation parameters for TIDs

After normalizing the disturbance patterns and removing isolated disturbances using filtering criteria, what remains are TID structures represented by ellipses. Figure 7 shows the calculation method for propagation parameters between adjacent TID waves. To mathematically quantify these wave-like disturbances, this study follows the same definition of the pixel coordinate system as in the *OpenCV* library, which is obtained by rotating the traditional Cartesian coordinate system clockwise by 90°, with the south direction as the positive x-axis direction and the east direction as the positive y-axis direction. The green represents disturbance structure *i*, and the blue represents disturbance structure *j*.

The distance D_{ctc} between the centroids of two adjacent disturbed structures can be calculated by the distance between two points equation:

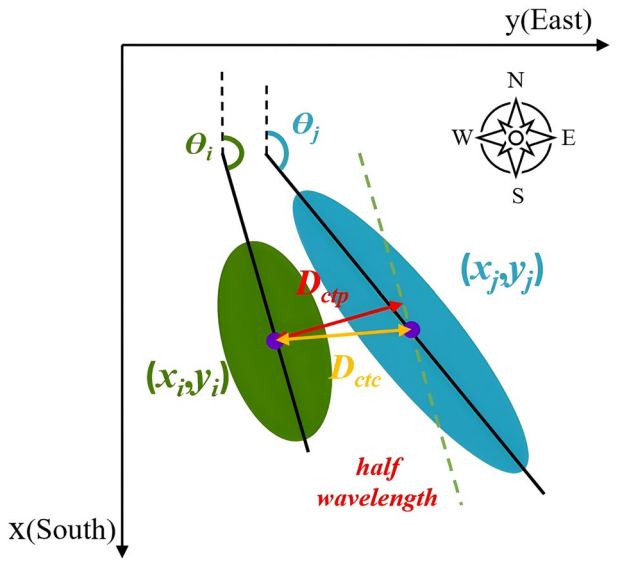

Fig. 7 Schematic diagram of propagation parameters calculation between adjacent wave-like structures of TIDs

$$D_{ctc}^{ij} = \sqrt{(x_i - x_j)^2 + (y_i - y_j)^2} \tag{7}$$

However, the wavelength of TIDs is not equal to the distance between the centers of two waves but should be the distance in the direction of propagation. To derive the wavelength of TIDs, assume the center coordinates of the target disturbance structure are (x_i, y_i) with a major axis angle of θ_i, and the center coordinates of the next disturbance structure are (x_i, y_i) with a major axis angle of θ_j. Then, draw a line parallel to the major axis of disturbance *i* through the center of disturbance *j*. The equation of this parallel line is as follows:

$$y - y_j = \tan\theta_i(x - x_j) \tag{8}$$

The general form of Eq. (9) converted into a linear equation is as follows:

$$\tan\theta_i x - y + (y_j - \tan\theta_i x_j) = 0 \tag{9}$$

Then the distance D_{ctp} from perturbation *i* to perturbation *j* can be calculated by the point-to-straight line equation:

$$D_{ctp}^{ij} = \frac{\left|\tan\theta_i x_i - y_i + y_j - \tan\theta_i x_j\right|}{\sqrt{(\tan\theta_i)^2 + (-1)^2}} \tag{10}$$

The D_{ctp}^{ij} describes the calculation of the wavelength between adjacent disturbances. However, when conducting calculations for the entire DTEC map, the distribution of disturbances is more dispersed, making it impossible to determine which two disturbances are adjacent. This study utilizes the n-dimensional Euclidean distance to filter out the neighboring disturbance structures of the target disturbance. Specifically, the disturbance *j* that minimizes FC_i is considered the adjacent disturbance to disturbance *i*. Additionally, a judgment is made: if disturbances *i* and *j* are not both peaks or both troughs, the distance D_{ctp} from disturbance *i* to disturbance *j* is half a wavelength; if disturbances *i* and *j* are both peaks or both troughs, D_{ctp} is a full wavelength. The formula for calculating the TIDs propagation parameters of the full DTEC map is as follows:

$$\begin{cases} Wavelength = \frac{\sum_{k=1}^{n} D_{ctp}^{k} \cdot index(k)}{n} \\ Extension\ length = \frac{\sum_{k=1}^{n} a^k}{n} \\ Extension\ angle = \frac{\sum_{k=1}^{n} \left|180° - \theta^k\right|}{n} \end{cases} \tag{11}$$

where *n* represents the number of disturbances in the DTEC map, *k* denotes a specified disturbance; D_{tcp}^{k} is the distance from the *k*th disturbance to its adjacent disturbance; *index*(*k*) represents the characteristic index of this disturbance, where *index*(*k*) is 1 if the adjacent disturbance is a peak or a trough,

and $index(k)$ is 2 if it is not; a^k is the major axis of the kth disturbance structure and θ^k is the angle between the major axis of the kth disturbance structure and the north direction.

Results and discussion

This section first discusses the training results of Cascade Mask R-CNN and Mask R-CNN models. Then, it shows the results of wave disturbance after normalization processing and removal of isolated disturbances. Finally, the propagation parameters of TIDs are calculated.

Model training results

To further enhance model training, this study simultaneously used the Mask R-CNN and the Cascade Mask R-CNN model to extract TIDs and compared the results. Figure 8 illustrates the variation of bounding box and mask accuracy with epochs during the training of both models. In Fig. 8, the horizontal axis represents the number of training epochs, while the vertical axes (bbox_mAP_50 and segm_mAP_50) denote the accuracies of the bounding boxes and masks, respectively. The blue and yellow lines represent the training curves of Mask R-CNN and Cascade Mask R-CNN, and the red dots indicate the epochs with the highest accuracy during the training process for both networks. Figure 8a illustrates that the training curve of Cascade Mask R-CNN consistently outperforms that of Mask R-CNN, with the bounding box

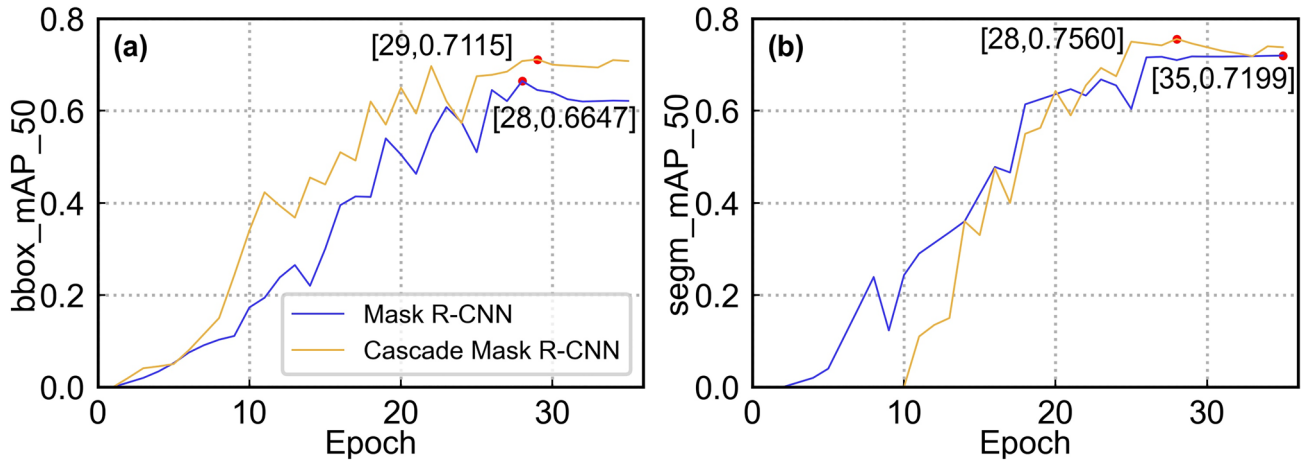

Fig. 8 Bounding box and mask accuracy of Mask R-CNN and Cascade Mask R-CNN models

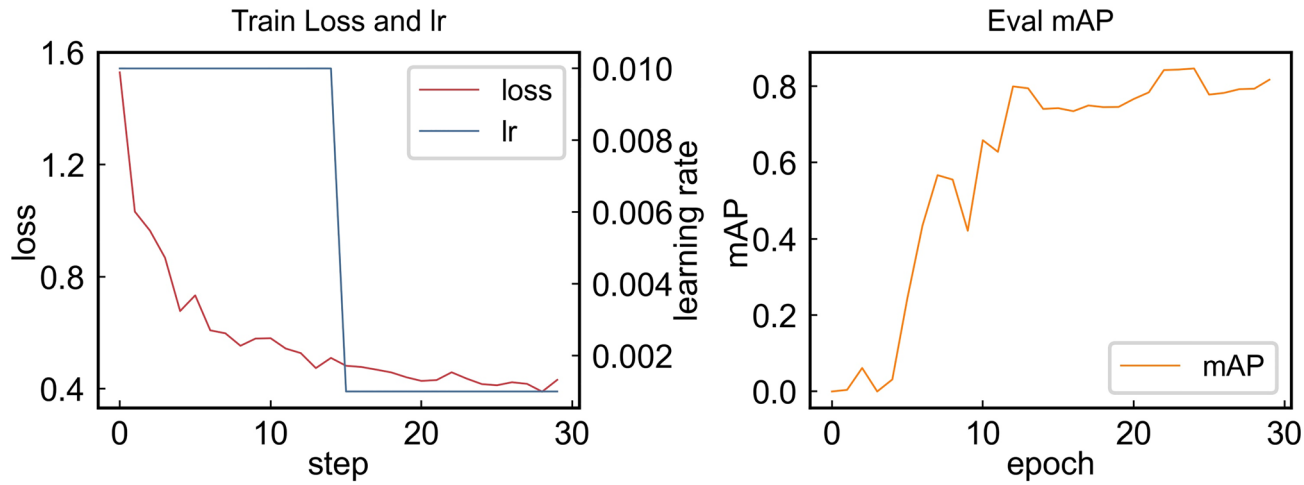

Fig. 9 Loss and mAP of the European regional model with different learning rate settings

accuracy reaching 71.15%, approximately 4.7% higher than that of Mask R-CNN. Figure 8b displays the mask accuracy of the two models, with the Cascade Mask R-CNN achieving an accuracy of 75.6%, representing an improvement of around 3.6% compared to the Mask R-CNN model.

In model training, different parameters have varying impacts on the results. Therefore, adjusting appropriate parameters can improve model accuracy while accelerating convergence. Figures 9 and 10 show the loss and mAP curves for the European and global TIDs datasets under different learning rate settings, respectively. As seen in Fig. 9, for the European region, when the number of iterations is set to 30, the batch size is 2, the learning rate is 0.01, the momentum is set to 0.9, weight decay is 0.00001, and the learning rate decay mechanism reduces the learning rate to one-tenth of its original value after 15 iterations, the model achieves optimal results. The bounding box accuracy (mAP_{50}) reaches 85.11%, and the mask accuracy reaches 79.34%. Figure 10 demonstrates that for the global region, when the number of iterations is set to 30, the batch size is 2, the learning rate is 0.005, the momentum is 0.9, weight decay is 0.00001, and the learning rate decay mechanism reduces the learning rate to one-fifth of its original value after the 10th and 19th iterations, the model yields a bounding box accuracy (mAP_{50}) of 66.68% and a mask accuracy of 73.37%.

Table 1 further summarizes the bounding box accuracy of models for different regions after training. As shown in Table 1, the mAP_{50} values for the European and global region models are 85.11% and 66.68%, respectively. The lower mAP_{50} for the global region could be attributed to the relative scarcity of global LSTIDs events, which may result in a slightly weaker generalization ability for the model. For both the European and global regions, the mAP_{small} value is − 1, indicating that no accuracy data is available for small bounding boxes. This suggests that the detected disturbance boundaries were relatively large, and no small bounding boxes were identified. This phenomenon may be related to image resolution as well as the specific disturbance characteristics and observation conditions in different regions.

Table 2 shows the mask accuracy of the models for different regions after training. As shown in Table 2, when the IoU threshold is set to 50%, the mAP_{50} for the European region model is 79.34%, which is approximately 6% lower than

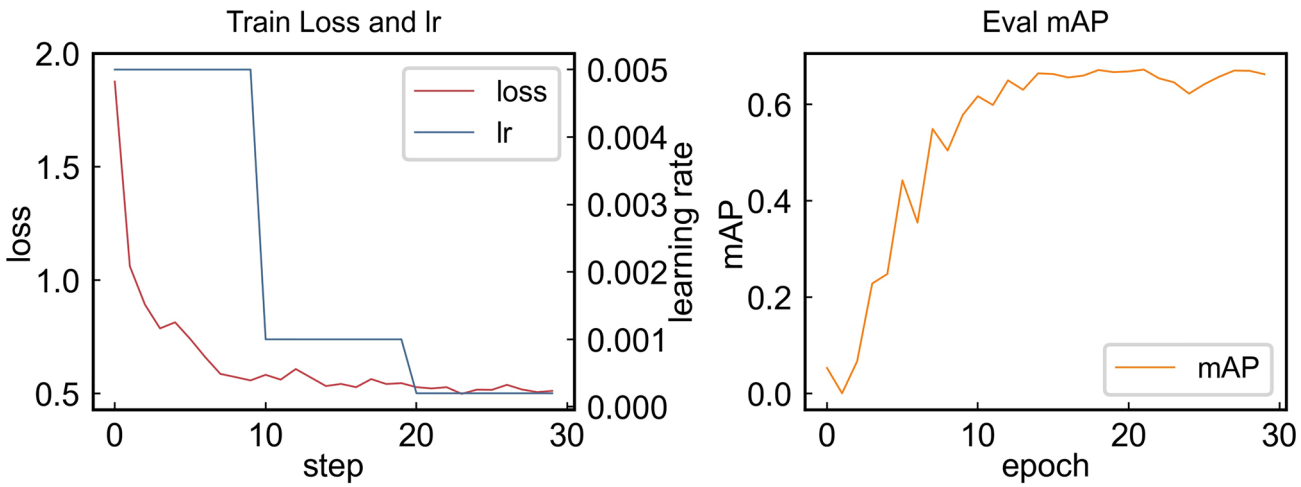

Fig. 10 Loss and accuracy mAP of the global model with different learning rate settings

Table 1 Model bounding box training accuracies for the European and global region models

Area	$mAP_{50:5:95}$	mAP_{50}	mAP_{75}	mAP_{small}	mAP_{medium}	mAP_{large}
Europe	0.4189	0.8511	0.3286	− 1.0000	0.3792	0.5626
Global	0.3372	0.6668	0.3396	− 1.0000	0.3613	0.3572

Table 2 Model mask training accuracies for the European and global region models

Area	$mAP_{50:5:95}$	mAP_{50}	mAP_{75}	mAP_{small}	mAP_{medium}	mAP_{large}
Europe	0.4407	0.7934	0.4254	− 1.0000	0.3817	0.6272
Global	0.4007	0.7337	0.4792	− 1.0000	0.44616	0.4787

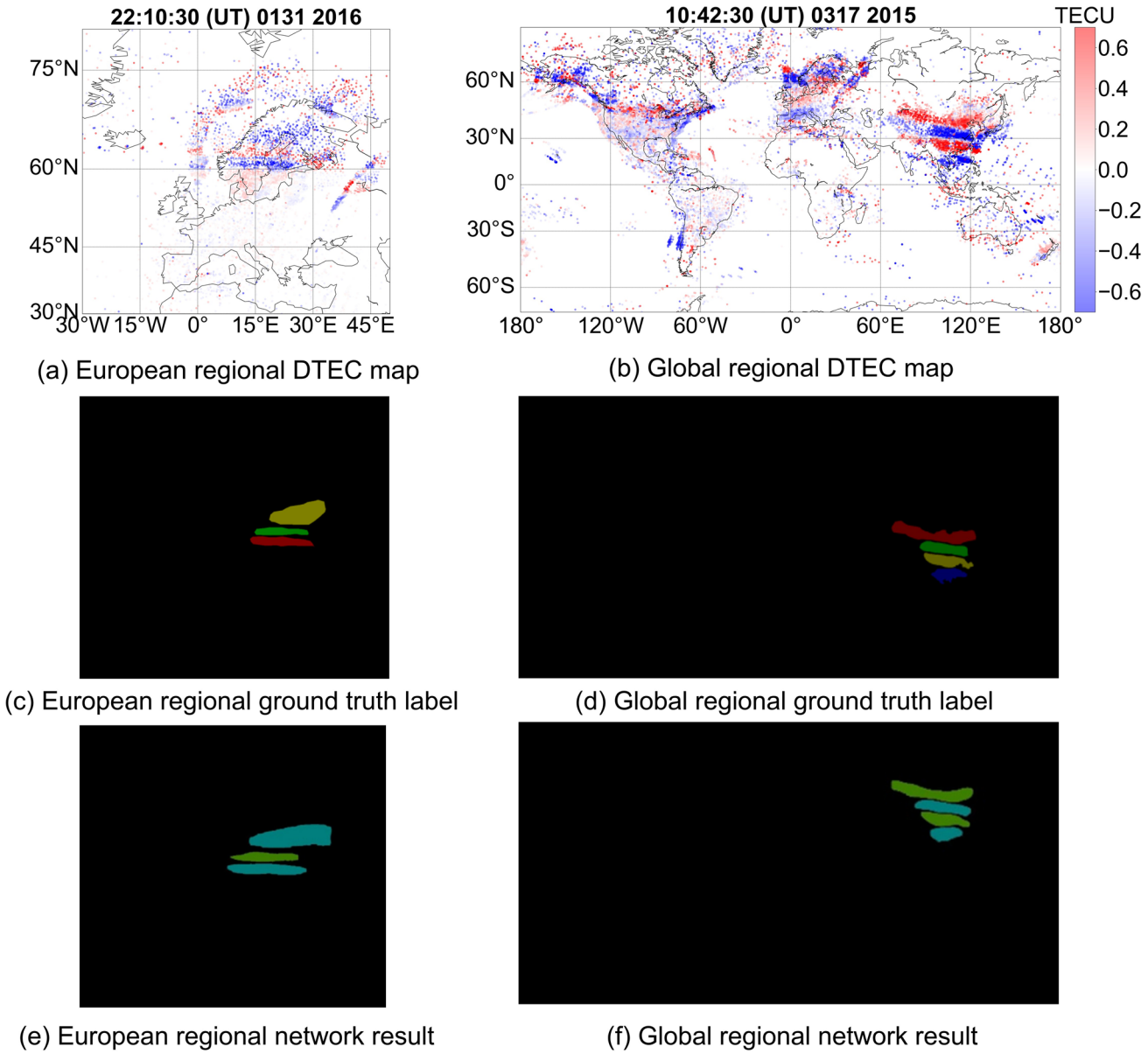

Fig. 11 ionospheric disturbance extraction results for the European regional (left) and global-scale (right) models

the bounding box accuracy. For the global region model, the mAP_{50} is 73.37%, which represents an 8% improvement over the bounding box accuracy. Similar to the bounding box results, no small masks were detected in either the European or global regions.

TIDs extraction and propagation parameter calculation

By processing the DTEC maps in the European region using the trained model, the TIDs components contained within the maps can be extracted. Figure 11 illustrates the ionospheric disturbance extraction results for both the European and global region models. Figure 11a, b display the original DTEC maps of the European and global regions, respectively. Figure 11c, d show the manually annotated labels for the European and global region models, which are considered ground-truth masks. Figure 11e, f present the output results from the networks of the European and global region models, respectively. To better distinguish the crest and trough structures, the same colors are used to label the same categories in the mask display, with blue and green representing trough and crest regions, respectively. As seen in Fig. 11, the network training results for both the European and global region models are quite effective, with the extracted ionospheric disturbance information closely

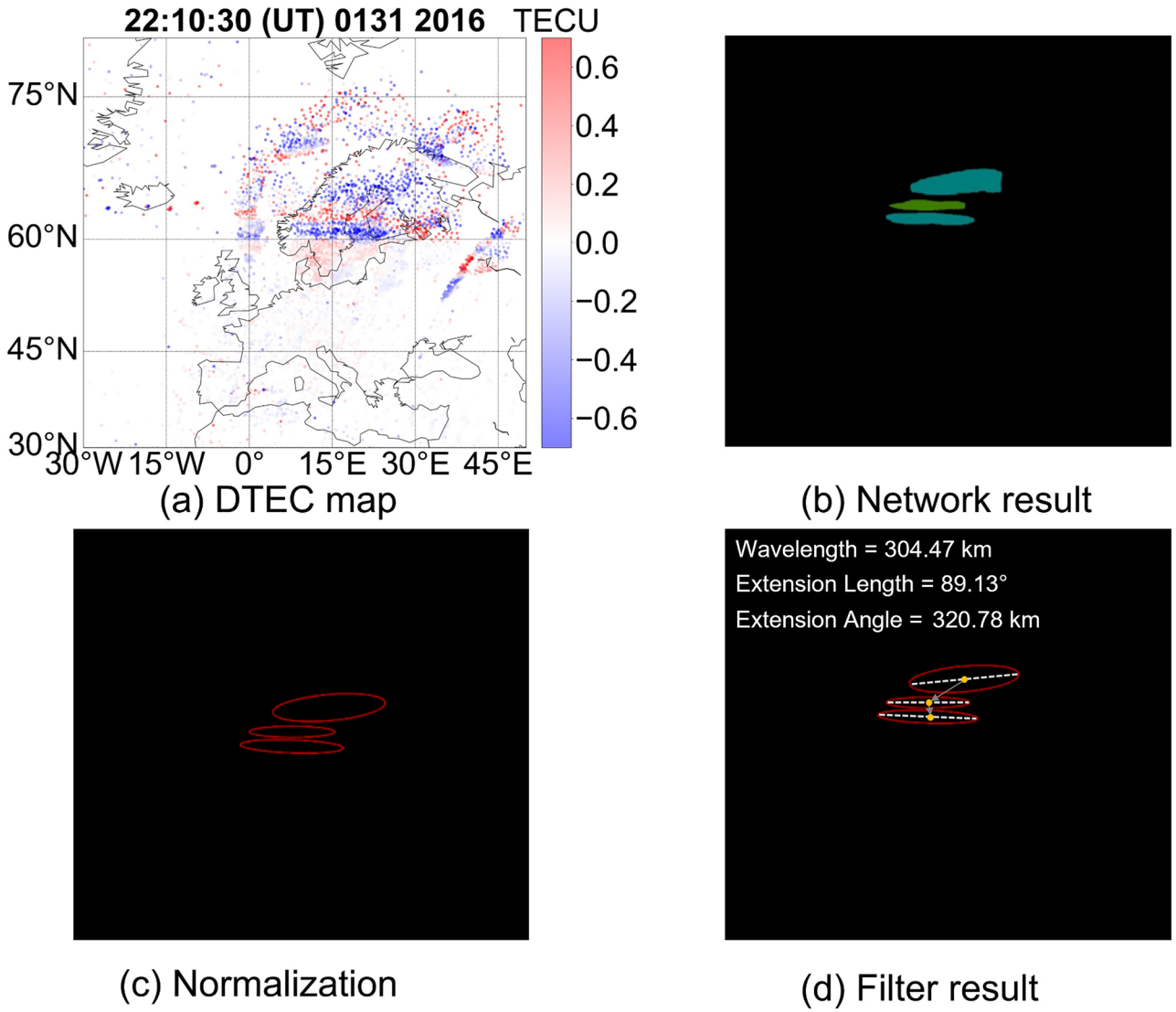

Fig. 12 MSTID extraction results in the European regional area

matching the manually annotated labels. The crest and trough structures are clearly visible in both regions.

Figure 12 demonstrates the extraction and parameter calculation results of MSTIDs in the European region. At the time shown in Fig. 12, an MSTID event was observed in the European region. Figure 12a shows the original DTEC map, while Fig. 12b presents the mask image of the disturbance extraction result from the network output. Figure 12c depicts the image after being processed using a shape normalization method, and Fig. 12d shows the result after applying the isolated disturbance removal method based on filtering criteria. Since no isolated disturbances were present in Fig. 12, no disturbances were filtered out, and thus, there is no difference between Fig. 12c, d. After parameter calculation, the MSTIDs wavelength was determined to be 304.47 km, the propagation angle of the disturbance was 89.13°, and the disturbance extension length was 320.78 km. These results align well with the actual MSTIDs propagation characteristics.

Similar to Fig. 12, Fig. 13 shows the extraction and parameter calculation results for LSTIDs in the global region. At the time depicted in Fig. 13, an LSTIDs event occurred globally, and alternating crest and trough structures were observable in the China region. As in Fig. 12, there were no isolated disturbances in Fig. 13, so no disturbances were filtered out. By calculating the disturbance propagation parameters, the wavelength of the ionospheric LSTIDs in Fig. 13 was determined to be 1262.62 km, the propagation angle of the disturbance was 94.67°, and the disturbance extension length was 1343.50 km. These results align well with the actual LSTIDs propagation characteristics.

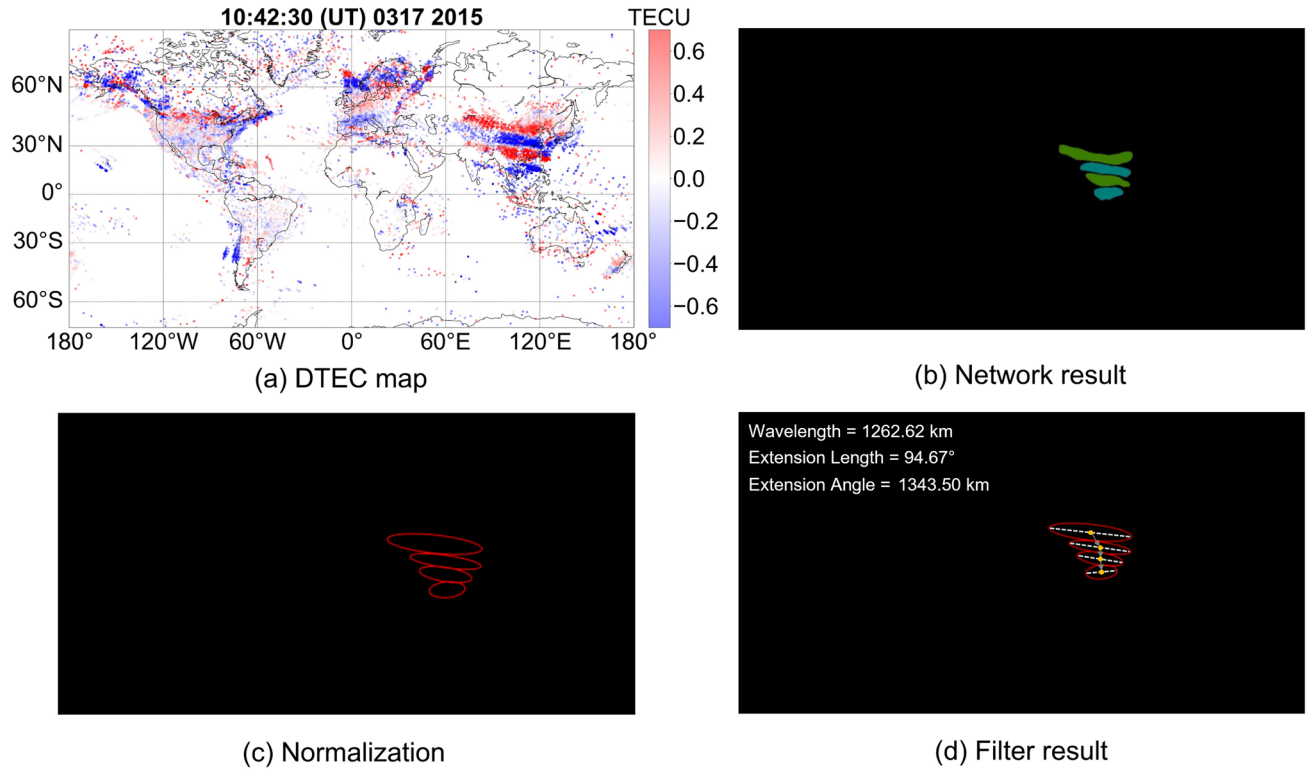

Fig. 13 LSTID extraction results in the global area (without isolated perturbations)

Figure 14 shows the propagation parameter calculation results for all MSTIDs in the European region of the dataset. The wavelength statistics in Fig. 14a show an average wavelength of 301.79 km (standard deviation of 78.87 km), with the overall distribution ranging from 100 to 500 km, and the highest frequency occurring in the 300–325 km range. The disturbance extent length results in Fig. 14b show an average extent length of 331.54 km (standard deviation of 107.81 km), with more than 70% of the disturbances concentrated in the 200–400 km range. The disturbance extent angle results in Fig. 14c show an average extent angle of 82.25° (standard deviation of 16.02°). Since the wave's extension direction is perpendicular to its propagation direction, the disturbance extent angle represents the angle between the disturbance extension direction and the north direction. As shown in Fig. 14c, the disturbance extension angles of MSTIDs in the European region are concentrated between 50° and 100°, with a peak direction around 80°–90°, indicating that the propagation direction is primarily north-to-south. The occurrence time results in Fig. 14d show that MSTIDs in the European region occur predominantly between 19:00 UTC and 23:00 UTC (local time approximately 20:00–24:00), indicating a higher probability of MSTID occurrence in the evening to midnight hours.

Conclusions

TIDs detection and propagation parameter calculation are essential foundations for ionospheric disturbance monitoring and early warning. In this study, based on the deep learning instance segmentation multi-stage method Cascade Mask R-CNN model and using high spatio-temporal resolution GNSS observation data, an intelligent method for TIDs wave disturbance recognition is proposed. The paper provides a detailed introduction to the deep learning-based ionospheric disturbance intelligent recognition method and related steps, including TIDs dataset creation, model training strategies, and TIDs propagation parameter calculation methods. By comparing the instance segmentation results of the Cascade Mask R-CNN model with the classical Mask R-CNN model on global LSTIDs and European MSTIDs data, the study demonstrates superior performance of the Cascade Mask R-CNN in both image processing accuracy and training convergence speed. Specifically, the Cascade Mask R-CNN improves bounding box accuracy by approximately 4.7% and mask accuracy by approximately 3.6%. The bounding box accuracy (mAP_{50}) for the European region model reaches 85.11%, while mask accuracy reaches 79.34%. For the global region model, the bounding box accuracy (mAP_{50}) reaches 66.68%, with a mask accuracy of 73.37%. Additionally, using the least squares ellipse fitting method, the

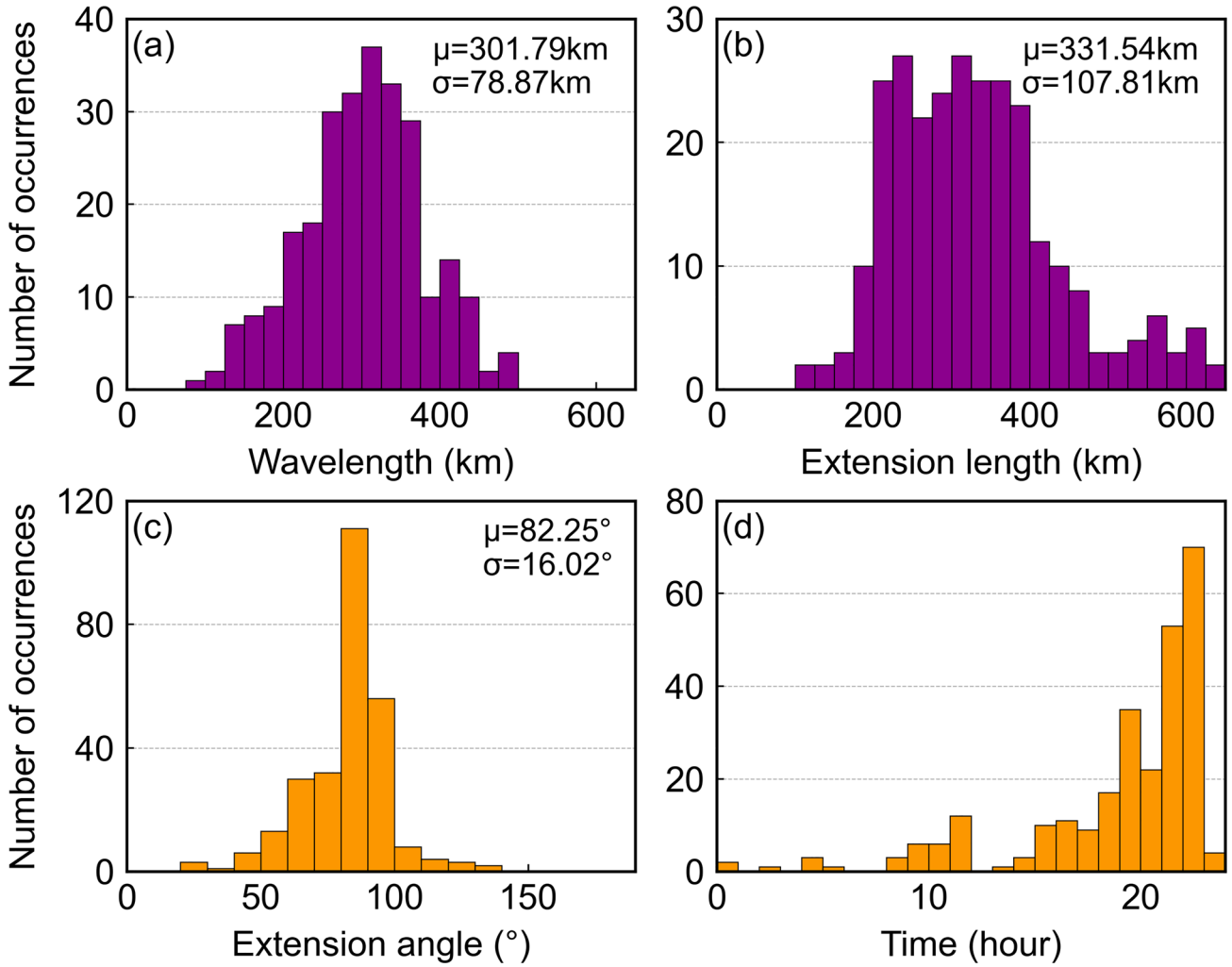

Fig. 14 Distribution of MSTID propagation parameters in the European region of the dataset

study normalizes irregular disturbance shapes. Isolated disturbances are filtered and removed using a filtering criterion and a nonlinear programming solver. Results indicate that setting the threshold T_1 to 40 effectively filters out isolated disturbances while retaining TIDs components. Furthermore, the TIDs propagation parameter calculations from the DTEC maps in different regions using the Cascade Mask R-CNN closely align with the actual results. It is worth noting that our method is currently limited to detecting TIDs as plane waves and is not applicable to the complex upward propagation phenomena of MSTIDs induced by events such as solar eclipses, tsunamis, and typhoons. In addition, although this study focuses on the detection accuracy of wave-like structures, we acknowledge that a deeper analysis of the model's uncertainty and confidence is important to evaluate the reliability of the detection results. In future work, we aim to incorporate uncertainty quantification into our framework to further enhance the interpretability and robustness of the model's outputs. As a future outlook, we also hope to develop our approach further when a sufficient amount of three-dimensional electron density data capable of describing MSTIDs structures becomes available.

Acknowledgements This research was funded by the National Natural Science Foundation of China (no. 42230104, no. 42388102), the Fundamental Research Funds for the Central Universities (no. 2042025kf0026) and the Key R&D Program Projects in Hubei Province (no. 2022BAA053). The numerical calculations have been done on the supercomputing system in the Supercomputing Center of Wuhan University.

Author contributions XR and PZ conceived and defined the research theme. PZ and XL processed most of the data and plotted all the graphs. XL and LJ conducted the data analysis and wrote the manuscript. AA revised the grammatical structure of the manuscript. XZ and XR revised the final manuscript. All authors read and approved the final manuscript.

Data availability The line-of-sight TEC data are available in National Oceanic and Atmospheric Administration (NOAA's) National Geophysical Data Center: http://cedar.openmadrigal.org/. The dTEC maps over Japan are available in NICT: https://aer-nc-web.nict.go.jp/GPS/GEONET/MAP/. The open-source software *Labelme* is available in Github: https://github.com/wkentaro/labelme. The instance segmentation model Cascade Mask R-CNN and Mask R-CNN are in Github: https://github.com/anonymoussss/Cascade-Mask-RCNN and https://github.com/matterport/Mask_RCNN.

Declarations

Conflict of interest The authors declare no competing interests.

References

Astafyeva E (2019) Ionospheric detection of natural hazards. Rev Geophys 57(4):1265–1288. https://doi.org/10.1029/2019RG000668

Behnke R (1979) F layer height bands in the nocturnal ionosphere over Arecibo Journal of Geophysical Research: Space Phys 84(A3):974–978. https://doi.org/10.1029/JA084iA03p00974

Borries C, Ferreira AA, Nykiel G, Borges RA (2023) A new index for statistical analyses and prediction of travelling ionospheric disturbances. J Atmos Solar Terr Phys 247:106069. https://doi.org/10.1016/j.jastp.2023.106069

Brissaud Q, Astafyeva E (2022) Near-real-time detection of co-seismic ionospheric disturbances using machine learning. Geophys J Int 230(3):2117–2130. https://doi.org/10.1093/gji/ggac167

Cai Z, Vasconcelos N (2019) Cascade R-CNN: high quality object detection and instance segmentation. IEEE Trans Pattern Anal Mach Intell 43(5):1483–1498. https://doi.org/10.1109/TPAMI.2019.2956516

Cherniak I, Zakharenkova I (2018) Ionospheric total electron content response to the great American solar eclipse of 21 August 2017. Geophys Res Lett 45(3):1199–1208. https://doi.org/10.1002/2017GL075989

Efendi E, Arikan F (2017) A fast algorithm for automatic detection of ionospheric disturbances: DROT. Adv Space Res 59(12):2923–2933. https://doi.org/10.1016/j.asr.2017.03.018

Figueiredo CAOB, Wrasse CM, Takahashi H, Otsuka Y, Shiokawa K, Barros D (2017) Large-scale traveling ionospheric disturbances observed by GPS dTEC maps over North and South America on Saint Patrick's Day storm in 2015 Abstract Key Points Journal of Geophysical Research: Space Phys 122(4):4755–4763. https://doi.org/10.1002/2016JA023417

Frissell NA, Kaeppler SR, Sanchez DF, Perry GW, Engelke WD, Erickson PJ, Coster AJ, Ruohoniemi JM, Baker JBH, West ML (2022) First observations of large scale traveling ionospheric disturbances using automated amateur radio receiving networks. Geophys Res Lett 49(5):e2022GL097879. https://doi.org/10.1029/2022GL097879

Fuso F, Crocetti L, Ravanelli M, Soja B (2024) Machine learning-based detection of TEC signatures related to earthquakes and tsunamis: the 2015 Illapel case study Abstract GPS Solutions 28(3). https://doi.org/10.1007/s10291-024-01649-z

Girshick R (2015) Fast R-CNN. In: Proceedings of the IEEE international conference on computer vision, pp 1440–1448. https://doi.org/10.1109/ICCV.2015.169

Guerra M, Cesaroni C, Ravanelli M, Spogli L (2024) Travelling ionospheric disturbances detection: a statistical study of detrending techniques, induced period error and near real-time observables. J Space Weather Space Clim 14:17. https://doi.org/10.1051/swsc/2024017

He K, Gkioxari G, Dollár P, Girshick R (2017) Mask R-CNN. In: Proceedings of the IEEE international conference on computer vision, pp 2961–2969. https://doi.org/10.1109/ICCV.2017.322

Hernández-Pajares M, Juan JM, Sanz J, Aragón-Àngel A (2012) Propagation of medium scale traveling ionospheric disturbances at different latitudes and solar cycle conditions. Radio Sci 47(06):1–22. https://doi.org/10.1029/2011RS004951

Hines CO (1960) Internal atmospheric gravity waves at ionospheric heights. Can J Phys 38(11):1441–1481. https://doi.org/10.1029/GM018p0248

Huang F, Dou X, Lei J, Lin J, Ding F, Zhong J (2016) Statistical analysis of nighttime medium-scale traveling ionospheric disturbances using airglow images and GPS observations over central China. J Geophys Res Space Phys 121(9):8887–8899. https://doi.org/10.1002/2016JA022760

Huang F, Lei J, Dou X (2017) Daytime ionospheric longitudinal gradients seen in the observations from a regional BeiDou GEO receiver network. J Geophys Res Space Phys 122(6):6552–6561. https://doi.org/10.1002/2017JA023881

Hunsucker RD (1982) Atmospheric gravity waves generated in the high-latitude ionosphere: a review. Rev Geophys 20(2):293–315. https://doi.org/10.1029/RG020i002p00293

Li W, Jiang Y (2024) Equatorial plasma bubble model and integrity risk evaluation for ground based augmentation system in Hong Kong Abstract. Satell Navig 5(1):32. https://doi.org/10.1186/s43020-024-00154-5

Kamogawa M, Orihara Y, Tsurudome C, Tomida Y, Kanaya T, Ikeda D, Gusman RA, Kakinami Y, Liu JY, Toyoda A (2016) A possible space-based tsunami early warning system using observations of the tsunami ionospheric hole. Sci Rep 6(1):37989. https://doi.org/10.1038/srep37989

Kelley MC (2009) The Earth's ionosphere: plasma physics and electrodynamics. Academic Press

Koucká Knížová P, Laštovička J, Kouba D, Mošna Z, Podolská K, Potužníková K, Šindelářová T, Chum J, Rusz J (2021) Ionosphere influenced from lower-lying atmospheric regions. Front Astron Space Sci 8:651445. https://doi.org/10.3389/fspas.2021.651445

Lai C, Xu J, Lin Z, Wu K, Zhang D, Li Q, Sun L, Yuan W, Zhu Y (2023) Statistical characteristics of nighttime medium-scale traveling ionospheric disturbances from 10-years of airglow observation by the machine learning method. Space Weather 21(5):e2023SW003430. https://doi.org/10.1029/2023SW003430

Le X, Ren X, Mei D, Liu H, Zhang X (2024) Occurrence and characteristics of medium-scale traveling ionospheric disturbances observed by BeiDou GEO satellites over Hong Kong. J Geophys Res Space Phys 129(6):e2024JA032510. https://doi.org/10.1029/2024JA032510

Liu P, Yokoyama T, Fu W, Yamamoto M (2022) Statistical analysis of medium-scale traveling ionospheric disturbances over japan based on deep learning instance segmentation. Space Weather 20(7):e2022SW003151. https://doi.org/10.1029/2022SW003151

Luhrmann F, Park J, Wong WK, Corcoran F, Lewis C (2022) Detecting traveling ionospheric disturbances with LSTM based anomaly detection. In: Proceedings of the 35th international technical meeting of the satellite division of The Institute of Navigation (ION GNSS+ 2022), pp 3002–3011. https://doi.org/10.33012/2022.18343

Luhrmann F, Park J, Wong WK, Martire L, Krishnamoorthy S, Komjáthy A (2025) Detection of ionospheric disturbances with a sparse GNSS network in simulated near-real time Mw 7.8 and Mw 7.5 Kahramanmaraş earthquake sequence. GPS Solut 29(1):1–12. https://doi.org/10.1007/s10291-024-01808-2

Martire L, Krishnamoorthy S, Vergados P, Romans LJ, Szilágyi B, Meng X, Anderson LA, Komjáthy A, Bar-Sever YE (2023) The GUARDIAN system—a GNSS upper atmospheric real-time

disaster information and alert network. GPS Solut 27(1):32. https://doi.org/10.1007/s10291-022-01365-6
Minaee S, Boykov Y, Porikli F, Plaza A, Kehtarnavaz N, Terzopoulos D (2022) Image segmentation using deep learning: a survey. IEEE Trans Pattern Anal Mach Intell 44(7):3523–3542. https://doi.org/10.1109/TPAMI.2021.3059968
Oludehinwa IA, Velichko A, Ogunsua BO, Olusola OI, Odeyemi OO, Njah AN, Ologun OT (2022) Dynamical complexity response in traveling ionospheric disturbances across Eastern Africa sector during geomagnetic storms using neural network entropy. J Geophys Res Space Phys 127(9):e2022JA030630. https://doi.org/10.1029/2022JA030630
Pi X, Mannucci AJ, Lindqwister UJ, Ho CM (1997) Monitoring of global ionospheric irregularities using the worldwide GPS network. Geophys Res Lett 24(18):2283–2286. https://doi.org/10.1029/97GL02273
Ravanelli M, Constantinou V, Liu H, Bortnik J (2024) Exploring AI progress in GNSS remote sensing: a deep learning based framework for real-time detection of earthquake and tsunami induced ionospheric perturbations. Radio Sci 59:e2024RS008016. https://doi.org/10.1029/2024RS008016
Ravanelli M, Occhipinti G, Savastano G, Komjathy A, Shume EB, Crespi M (2021) GNSS total variometric approach: first demonstration of a tool for real-time tsunami genesis estimation. Sci Rep 11(1):3114. https://doi.org/10.1038/s41598-021-82532-6
Ren S, He K, Girshick R, Sun J (2017) Faster R-CNN: towards real-time object detection with region proposal networks. IEEE Trans Pattern Anal Mach Intell 39(6):1137–1149. https://doi.org/10.1109/TPAMI.2016.2577031
Ren X, Le X, Mei D, Liu H, Zhang X (2024) IROTI: a new index to detect and identify traveling ionospheric disturbances and equatorial plasma bubbles. GPS Solut 28(1):1–13. https://doi.org/10.1007/s10291-023-01545-y
Ren X, Mei D, Liu H, Zhang X (2022) Investigation on horizontal and vertical traveling ionospheric disturbances propagation in global-scale using GNSS and multi-LEO satellites. Space Weather 20(5):e2022SW003041. https://doi.org/10.1029/2022SW003041
Rideout W, Coster A (2006) Automated GPS processing for global total electron content data. GPS Solut 10:219–228. https://doi.org/10.1007/s10291-006-0029-5
Vierinen J, Coster AJ, Rideout WC, Erickson PJ, Norberg J (2016) Statistical framework for estimating GNSS bias. Atmos Meas Tech 9(3):1303–1312. https://doi.org/10.5194/amt-9-1303-2016
Wilken V, Kriegel M, Jakowski N, Berdermann J (2018) An ionospheric index suitable for estimating the degree of ionospheric perturbations. J Space Weather Space Clim 8:A19. https://doi.org/10.1051/swsc/2018008
Yang H, Monte-Moreno E, Hernández-Pajares M (2017) Multi-TID detection and characterization in a dense global navigation satellite system receiver network. J Geophys Res Space Phys 122(9):9554–9575. https://doi.org/10.1002/2017JA023988
Yang YM, Komanduru A, Garrison J (2023) Detection of atmospheric–ionospheric disturbances in TEC Time series from large GNSS networks using wavelet coherence. IEEE J Sel Topics Appl Earth Obs Remote Sens 16:5154–5172. https://doi.org/10.1109/JSTARS.2023.3276346
Zhang X, Ren X, Chen J, Zuo X, Mei D, Liu W (2022) Investigating GNSS PPP–RTK with external ionospheric constraints Abstract. Satell Navig 3(1):6. https://doi.org/10.1186/s43020-022-00067-1

Xiaodong Ren is currently a professor at Wuhan University. He obtained his B.Sc., Master, and Ph.D. degrees with distinction in Geodesy and Engineering Surveying at the School of Geodesy and Geomatics in Wuhan University in 2011, 2013, and 2017. His main research focuses on Muti-GNSS real-time precise positioning and ionospheric modeling.

Pengchong Zhao received his Bachelor's degree in 2022 and Master's degree in 2024 from the School of Geodesy and Geomatics at Wuhan University. His research during the master's program focused on ionospheric disturbance and deep learning.

Xuan Le is currently a Ph.D. candidate at Wuhan University. He received the B.Sc. and master's degrees from Wuhan University in 2021 and 2023, respectively. His current research focuses on the ionospheric monitoring, modeling and deep learning.

Linghuo Jian is currently a Ph.D. candidate at Wuhan University. He received his B.Sc. and master's degrees from Guizhou University in 2021 and 2024, respectively. His current research interests include ionospheric scintillation monitoring and GNSS reflectometry.

Ahmed Abdelaziz is currently a PhD candidate at Wuhan university (LIESMARS) since Sep, 2022 and teaching assistant in Benha Faculty of Engineering, Benha University, Egypt. He obtained his B.Sc., in civil engineering from Benha university in 2017, his master degree in SC and GNSS from Beihang university, Beijing, China in 2021. His current research focuses on the ionospheric modeling and deep learning.

Xiaohong Zhang is currently a professor at Wuhan University. He obtained his B.Sc., Master, and Ph.D. degrees with distinction in Geodesy and Engineering Surveying at the School of Geodesy and Geomatics in Wuhan University in 1997, 1999, and 2002. His main research interests include Precise Point Positioning and GNSS/INS.